Composite Structures 291 (2022) 115560

Contents lists available at ScienceDirect

Composite Structures

journal homepage: www.elsevier.com/locate/compstruct

A computationally efficient approach for generating RVEs of various inclusion/fibre shapes

Rajesh Nakka [a], Dineshkumar Harursampath [a,*], Mehtab Pathan [b], Sathiskumar A. Ponnusami [b,*]

[a] NMCAD Laboratory, Department of Aerospace Engineering, Indian Institute of Science, Bengaluru, Karnataka, India
[b] Aeronautics and Aerospace Research Centre, Department of Mechanical Engineering and Aeronautics, City, University of London, Northampton Square, London, United Kingdom

ARTICLE INFO

Keywords:
Fibre composites
Particulate composites
Microstructure
Micromechanics
Collision detection

ABSTRACT

A computationally efficient method for generating virtual periodic representative volume element (RVE), capable of handling arbitrary inclusion shapes, is developed. A universal collision/overlap detection and repair method is proposed, where each inclusion shape is represented as a union of n-Spheres (UnS). A constrained optimization problem is formulated and solved to remove inclusion overlaps; a closed-form solution is derived for calculating the degree of inclusions overlap and its gradient vector with respect to inclusion position. RVE generation is illustrated with circular, spherical, four non-circular and four non-spherical inclusion shapes. Computational efficiency is demonstrated using an elaborate RVE generation time study. The generated RVEs are evaluated using various statistical metrics; results confirm the random distribution of inclusions. Effective properties of RVEs, representing unidirectional composites, are determined using homogenization with various fibre cross-section shapes; obtained mechanical properties have shown transverse isotropy.

1. Introduction

Over the past few decades, composites presence is increasing significantly in various industries due to their superior properties, such as higher specific stiffness and strength. Evaluation of these properties (and damage behaviour) is a non-trivial task. They are controlled by multiple factors such as constituent material properties, the relative proportion of constituents, geometrical arrangement of inclusions and properties of the inclusion–matrix interface. Experimental and theoretical approaches exist for evaluating composite properties, but the former approach is prohibitive due to the enormous amount of human and capital resources involved in the process. In theoretical approaches, the material's representative volume element (RVE) is used to find effective properties. RVE is chosen to contain all the typical heterogeneities of the microstructure, and its constitutive behaviour is the same as that of the whole composite material. Among the different theoretical methods, finite element analysis based numerical homogenization has become very popular due to its capability in capturing microstructural morphology.

Large-scale manufacturing of composites leads to random placement of fibres instead of regular arrangement. It was observed that in the case of long fibre reinforced composites, RVE of regularly arranged inclusions can predict effective properties up to a reasonable accuracy, but it is not a good choice for damage predictions [1–4]. Also, the damage initiation strongly depends on the inter-fibre distances [5], so it is of interest to reproduce realistic inter-inclusion distance distribution in RVE. RVE dimensions also influence effective properties, so optimum RVE size is determined from the convergence study of its properties. For example, Trias et al. [6,7] suggested RVE side length as about 50 times fibre radius for carbon fibre reinforced polymer composites.

RVE can be generated, according to Bergmann et al. [8], broadly in three ways. One, microstructure reconstruction from images [9] using costly and time-consuming methods like X-ray tomography, digital image correlation. Two, the physical processes involved in manufacturing are simulated for getting a more realistic distribution of inclusions. These models simulate the position and orientation of the inclusions by modelling the resin flow [10,11]. Three, mimicking the actual microstructure morphology using geometrical methods [12,13] which is followed in the present work.

Random sequential adsorption (RSA) [14], also known as the hard-core model, is a simple and widely used approach for generating virtual RVEs. In this method, inclusions are placed randomly inside the RVE boundaries, one after the other, such that the new inclusion does not intersect with the previously placed inclusions until the required inclusion volume fraction is reached. RSA suffers from lower jamming limits [14,15], where the jamming limit is defined as the maximum inclusion volume fraction beyond which adding new inclusions is not

* Corresponding authors.
E-mail addresses: rajeshnakka@iisc.ac.in (R. Nakka), dineshkumar@iisc.ac.in (D. Harursampath), sathiskumar.ponnusami@city.ac.uk (S.A. Ponnusami).

https://doi.org/10.1016/j.compstruct.2022.115560
Received 1 December 2021; Received in revised form 9 March 2022; Accepted 4 April 2022
Available online 11 April 2022

possible. The jamming limit varies from RVE generation algorithm to algorithm and generating RVEs with volume fraction close to jamming limit would take significantly longer times [7]. For example, in the case of RSA, generating RVE of unidirectional composites, containing fibres of circular cross-section, with volume fractions greater than 50% would take very long time as the jamming occurs at about 54.6% inclusion volume fraction. Similarly, with RSA algorithm, jamming occurs at about 38% inclusion volume fraction in the case of particle reinforced composites of spherical shaped inclusions [14–16]. These limits are less than the inclusion volume fractions of high strength composites used in aerospace applications and theoretical limits(90% for UDCs and 74% for PRCs).

The lower jamming limit of RSA is due to poor space utilization, as the position of the accepted inclusions is fixed. In order to overcome this, one line of RVE generation models [12,17] are focused on perturbing accepted inclusions so that space is made to accommodate extra inclusions, thereby increasing the volume fraction limit. Recently, Wenlong Tian et al. [18] has coupled RSA with molecular dynamics simulations to generate RVE of mono-disperse particles (or spheres) with volume fractions greater than 50%. It is reported that this model [18] requires large computational times for volume fractions $\geq$50% or number of particles >100. Vaughan et al. [19], and Yang et al. [20] developed growth-based models where inclusions are added about an initial seed point (i.e., inclusion) at distances drawn from experimentally determined distributions. These models are able to reach fibre volume fractions up to about 65%. In another line of RVE generation models [21–23], instead of adding inclusions in series, all inclusions are arranged regularly upfront (for example, in rectangular or hexagonal patterns) then each of them is given random perturbation to achieve random distribution of inclusions. It is observed that it is challenging to obtain randomness at higher volume fractions using these methods [22].

In a more recent line of research [13,24,25], the required number of inclusions are randomly initialized, then inclusion overlaps are removed using an iterative procedure. Pathan et al. [13] used L-BFGS-B constrained optimization algorithm to minimize/eliminate the inclusion overlaps. Though it can generate RVEs with higher inclusion volume fractions, very high computational times are reported. Herráez et al. [25] considered inclusions as rigid bodies where overlaps are removed using repulsive force and momentum. This model,[25], generates RVEs of non-circular cross-sections with higher volume fractions in relatively shorter times. In this work, [25], RVE overlap is quantified using the area of inclusions intersection, which may not be easily determined for arbitrary inclusion shapes. Inclusion overlap checking, in general, is non-trivial for non-circular or non-spherical shapes, especially when they are arbitrarily aligned in the space [26,27]. Among the various existing methods, Gilbert–Johnson–Keerthi (GJK) algorithm [28] is more efficient for checking overlap of two arbitrary shapes in arbitrary positions. However, it is iterative in nature and intended for convex shapes. It can be extended to concave shapes as well by representing as a combination of convex shapes with increased complexity.

Machine Learning (ML) models [29–32] were developed to predict the effective properties of the composite materials. ML models, in general, are data-intensive and require a variety of data for better learning. In the case of RVE, this variety in data can be obtained from a broad spectrum of inclusion volume fractions, different inclusion shapes and different degrees of inclusion randomness. So, it is of interest to have an RVE generation algorithm handling these variations while maintaining the computational speed.

In this work, the RVE generation method based on bounds constrained optimization is proposed which works for any $2D$ and $3D$ inclusion shapes. An optimization problem is formulated to eliminate the inclusions overlap that occurred due to random initialization. As explained, algorithms like GJK can be used to efficiently detect the overlap between arbitrary shapes but finding the closed form expression for overlap cost and especially its gradient is not easy. Hence, in this work, a new method is developed for this purpose where each inclusion shape is represented as a union of n-Spheres(UnS). Also, the same UnS representation of a shape is used to determine its periodic copies. In Section 2, the proposed RVE generation methodology is described. Then, the method is applied to generate RVEs of five different $2D$ and five different $3D$ inclusion shapes in Section 3. Finally, in Sections 4 and 5, statistical and micromechanical validation is performed on the generated RVEs.

2. RVE generation methodology

RVE generation is accomplished majorly in two steps. First, inclusions are initialized randomly within the bounds of RVE, which may lead to inclusion-overlapping. Second, eliminating overlaps by inclusion repositioning while keeping them in contact with RVE. Fig. 1 shows all the steps involved in generating RVE of arbitrary inclusion shapes and a sample RVE generated using this algorithm.

2.1. Initialization

The inclusions are randomly placed, one after the other allowing overlaps, within the RVE boundary until the desired volume fraction is reached. In the present work, inclusion shapes are categorized as circular, spherical, non-circular and non-spherical shapes and their dimensions can be constant or drawn from a distribution of choice. Inclusions location and alignment are drawn from uniform distribution where each inclusion takes a position in the RVE domain with equal probability. For example, Eq. (1) shows optimization variables and their initialization formulae for rectangular or cubical shaped RVE. The set of optimization variables applicable for an inclusion depends on its geometry. Circular and spherical shapes need $(x,\ y)$ and $(x,\ y,\ z)$ respectively, as their orientations are immaterial so that the remaining terms can be set to zero or some arbitrary constant. Similarly, non-circular and non-spherical shapes need $(x,\ y,\ \theta)$ and $(x,\ y,\ z,\ \theta,\ \phi)$ respectively.

$$x = x_{min} + p(x_{max} - x_{min}) \tag{1a}$$

$$y = y_{min} + q(y_{max} - y_{min}) \tag{1b}$$

$$z = z_{min} + s(z_{max} - z_{min}) \tag{1c}$$

$$\theta = 2\pi u \tag{1d}$$

$$\phi = \cos^{-1}(2w - 1) \tag{1e}$$

where $p, q, s, u, w \in [0, 1]$ are drawn from uniform distribution, θ is azimuthal angle, ϕ is polar angle and $(x_{min},\ y_{min},\ z_{min},\ x_{max},\ y_{max},\ z_{max})$ are bounds of the RVE in $(x,\ y,\ z)$ directions. The choice of ϕ, in Eq. (1), is to ensure uniform distribution of points on the unit sphere, otherwise choosing $\phi = \pi w$ would cluster points near the poles [33]. Random initialization, as per Eq. (1), may lead to the overlapping of inclusions, which must be removed. For this purpose, an optimization-based iterative procedure for inclusions repositioning is presented in the next section.

2.2. Overlap elimination

In this section, all the steps involved in inclusion overlap elimination are presented in detail. Let i and j be any two inclusions with centres at $\mathbf{x}_i$ and $\mathbf{x}_j$ in a RVE domain Ω as shown in Fig. 2. The domain Ω is chosen as periodic to avoid gaps and overlaps when it is repeated in the space. Overlap between a pair of inclusions can be quantified either by using the intersection area or penetration distance along the line connecting centres. Due to its simplicity, we chose the distance-based approach. Let d_{ij} and $\overline{d_{ij}}$, respectively, denote centre-to-centre Euclidean distance and distance of the closest approach for i and j.

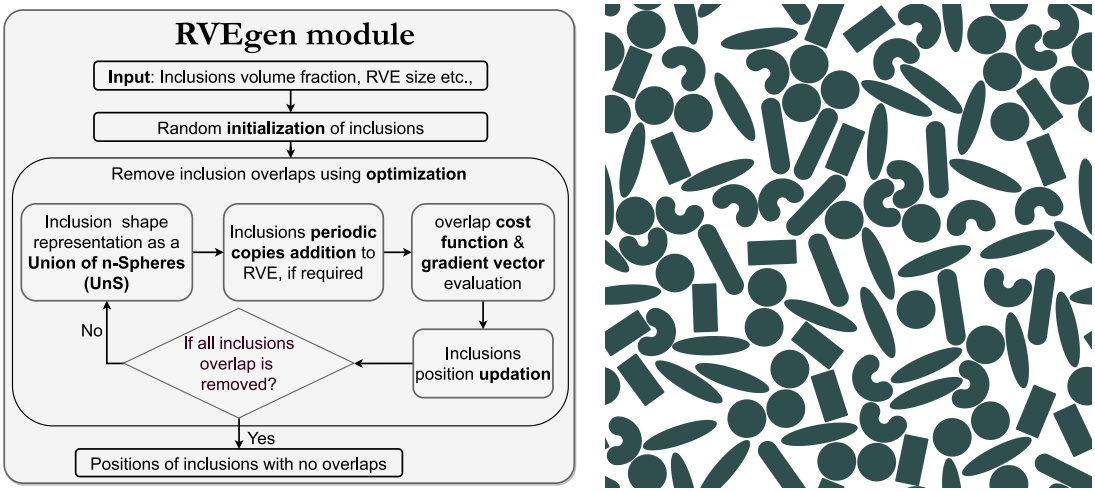

Fig. 1. RVE generation flow chart and a sample RVE of different inclusion shapes.

Here, the distance of the closest approach is defined as the centre-to-centre Euclidean distance when inclusions are just touching each other externally. Then, the total magnitude of inclusion overlap, f, in the RVE is defined as the cumulative sum of the overlap between all inclusion pairs as shown in Eq. (2)

$$f = \sum_{i=1}^{N-1}\sum_{j=i+1}^{N} \max(\overline{d}_{ij} - d_{ij}, 0) = \sum_{i=1}^{N-1}\sum_{j=i+1}^{N} (\overline{d}_{ij} - d_{ij})\mathbf{H}(\overline{d}_{ij} - d_{ij}) \tag{2}$$

where $\mathbf{H}(x)$ is Heaviside step function with unit value for all $x > 0$.

An optimization problem is formulated to minimize the total overlap, f, subject to the constraints that centre points, $\mathbf{x}_p$, of inclusions does not cross the RVE domain Ω.

$$\begin{aligned} &\text{Minimize} \quad f \\ &\text{subjected to } \mathbf{x}_p \in \Omega \end{aligned} \tag{3}$$

In Eq. (3), the RVE domain (Ω) can be in any shape of interest and it decides the nature of the constraint equations. In the present study, the RVE domain Ω is chosen as rectangular in $2D$ and cuboid in $3D$ as it ensures simple bounds on the spatial variables (x, y, z). Non-monotone spectral projected gradient (NMSPG) is used, in the present work, to solve the Eq. (3) as explained in Section 3 while any constrained optimization solver can be used.

2.2.1. Shape representation as a union of n-Spheres (UnS)

The overlap evaluation is a non-trivial task for non-circular and non-spherical shapes. In this section, we describe a novel, time-efficient/scalable approach to identify overlaps, thereby allowing our method to handle non-circular and non-spherical inclusion shapes. The idea is, overlap detection between a pair of arbitrary shapes can be converted to overlap detection between two groups of n-Spheres by representing inclusion shape as a union of n-Spheres (UnS). Here, the term "n-Sphere" implies a circle in 2D and a sphere in 3D, as used in mathematics. Fig. 3 shows the UnS representation of inclusion shapes considered in the present work. For example, checking the overlap between an ellipse and a rectangle requires finding the overlap between circles representing these two shapes. Overlap computation time is directly related to the number of n-Spheres used for each shape. Hence, using the minimum possible number of n-Spheres is desirable.

We proceed to find the centres and radii of n-Spheres to represent a shape. Let $\mathbb{C}_i$ and $\overline{\mathbb{C}}_i$ represent the equations of i^{th} shape boundary and a concentric outer curve around $\mathbb{C}_i$ with a thickness of d_{ss}, minimum distance between boundaries of any two shapes. Here, $\overline{\mathbb{C}}_i$ represents the region within which the boundary of the other shapes is barred from entering. Assuming that we know the position $\mathbf{x}_0$ and radii r_0 of the starting n-Sphere, then $\mathbf{x}_k$ and r_k of the successive n-Spheres are chosen such that the concentric n-Spheres of radius $r_k + d_{ss}$ would intersect on $\mathbb{C}_i$. This would ensure that the successive n-Spheres are separated by an optimum distance $d\mathbf{x}_k^*$. Overlap of inclusions may not be captured if n-Spheres are placed at a distance greater than $d\mathbf{x}_k^*$ because such a UnS may not represent the shape accurately. Also, n-Spheres closer than $d\mathbf{x}_k^*$ would unnecessarily increase the number of n-Spheres there by increasing the computation time. In Appendix A, formulae for finding the n-Spheres centre and radius are given for representing the ellipse/spheroid shape, the region between a pair of lines/planes separated by an angle 2β.

2.2.2. Periodic copies addition

In a micromechanical analysis of the RVE, applying periodic boundary conditions (PBC) is more advantageous over homogeneous boundary conditions [34,35]. In order to apply PBC, RVE must be continuous across its boundary when it is repeated in the space. To achieve this, if some part of an inclusion leaves the RVE boundary, then an *appropriate* number of its copies must be added to RVE at *appropriate* locations. Here, the number of periodic copies of an inclusion equals the number of RVE faces &/ edges &/ a vertex intersecting the inclusion. These periodic copies must be placed on the corresponding opposite face &/ edge &/ a vertex. For example, in 2D RVE, if an inclusion intersects two edges and a vertex, then three copies are added on two opposite edges and the opposite vertex. Finding intersections of RVE faces/edges/vertices with circular (in 2D) and spherical (in 3D) inclusion shapes is relatively simple. So, in this work, periodic copies are determined using the inclusions Union of n-Spheres (explained in the previous section) representation.

For each inclusion, the intersection of each of its n-Sphere with the RVE boundary is evaluated. Instances of inclusion's intersection with RVE is the same as the set of all n-Sphere's intersections with RVE faces &/ edges &/ a vertex. Accordingly, periodic copies of inclusions are added to RVE. As it involves running over each n-Sphere of each inclusion, filtering out boundary inclusions saves the computational effort. This can be done by checking the overlap of inclusion's bounding box with that of the RVE.

2.2.3. Cost function and gradient evaluation

Let inclusions i and j, as shown in Fig. 2, have N_i and N_j number of n-Spheres in their UnS form. The case of circular/spherical inclusion shape can be obtained by choosing $N_i = 1$ and $N_j = 1$. The cost of overlap between k^{th} n-Sphere of i^{th} inclusion and l^{th} n-Sphere of j^{th} inclusion is defined as

$$C_{ik,jl} = \max(0, \overline{d_{ik,jl}} - d_{ik,jl}) = \left(\overline{d_{ik,jl}} - d_{ik,jl}\right)\mathbf{H}(\overline{d_{ik,jl}} - d_{ik,jl}) \tag{4}$$

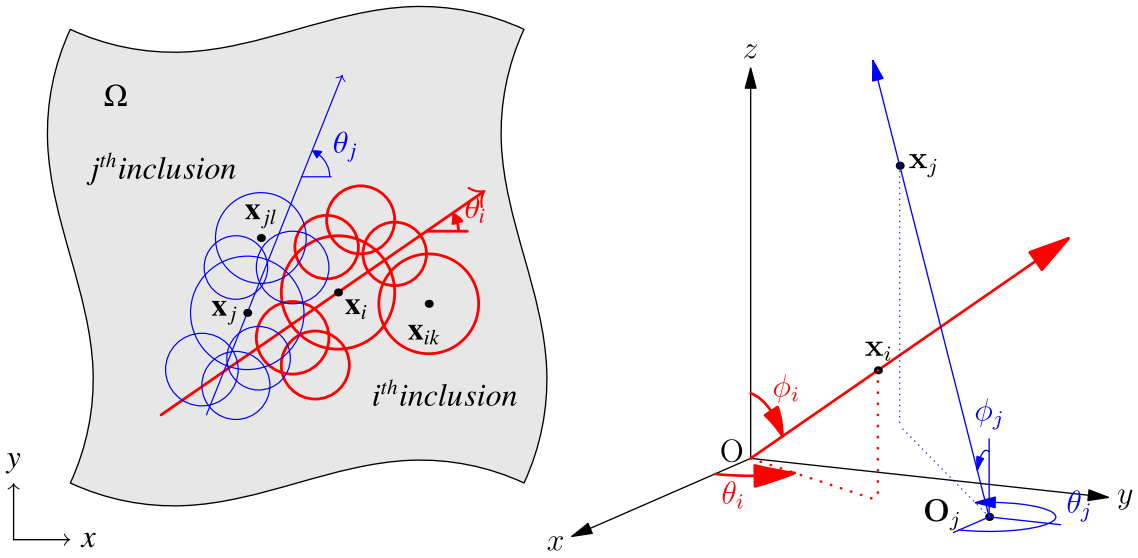

Fig. 2. Schematic of inclusions with n-Spheres.

with,

$$\begin{aligned}
\overline{d_{ik,jl}} &= r_{ik} + r_{jl} + d_{ss} \\
d_{ik,jl} &= \|\mathbf{x_{ik}} - \mathbf{x_{jl}}\|_2 \\
\mathbf{x_{ik}} &= (x_{ik}, y_{ik}, z_{ik}) = \mathbf{x_i} + \xi_{\mathbf{ik}}(\theta_\mathbf{i}, \phi_\mathbf{i}) \\
\mathbf{x_{jl}} &= (x_{jl}, y_{jl}, z_{jl}) = \mathbf{x_j} + \xi_{\mathbf{jl}}(\theta_\mathbf{j}, \phi_\mathbf{j})
\end{aligned} \tag{5}$$

where, $\mathbf{H}$ is the Heaviside step function, d_{ss} is the minimum surface-to-surface distance between any two inclusions, $\mathbf{x_{ik}}$ and $\mathbf{x_{jl}}$ are centres of k^{th} and l^{th} n-Spheres of i^{th} and j^{th} inclusions.

The total cost of overlap, f, for all N inclusions is given by

$$f(x, y, z, \theta, \phi) = \sum_{i=1}^{N-1} \sum_{j=i+1}^{N} \sum_{k=1}^{N_i} \sum_{l=1}^{N_j} C_{ik,jl}^2 \tag{6}$$

Gradient, the rate of change of the cost function, f, due to change in i^{th} inclusion variable $w_i \in \{x_i, y_i, z_i, \theta_i, \phi_i\}$ is evaluated as (refer to Appendix B for detailed derivation)

$$\nabla f = \left[\frac{\partial f}{\partial x_i} \quad \frac{\partial f}{\partial y_i} \quad \frac{\partial f}{\partial z_i} \quad \frac{\partial f}{\partial \theta_i} \quad \frac{\partial f}{\partial \phi_i}\right] \tag{7a}$$

$$= -2 \sum_{\substack{j=1 \\ \neq i}}^{N} \left\{ \sum_{k=1}^{N_i} \sum_{l=1}^{N_j} \frac{C_{ik,jl}}{d_{ik,jl}} \left[\Delta x_{ik,jl} \quad \Delta y_{ik,jl} \quad \Delta z_{ik,jl} \quad \Delta\theta_{ik,jl} \quad \Delta\phi_{ik,jl}\right] \right\} \tag{7b}$$

where,

$$\begin{aligned}
\Delta x_{ik,jl} &= x_{ik} - x_{jl} \\
\Delta y_{ik,jl} &= y_{ik} - y_{jl} \\
\Delta z_{ik,jl} &= z_{ik} - z_{jl} \\
\Delta\theta_{ik,jl} &= (y_i - y_{ik})\Delta x_{ik,jl} - (x_i - x_{ik})\Delta y_{ik,jl} \\
\Delta\phi_{ik,jl} &= \frac{z_i - z_{ik}}{\eta}(\Delta x_{ik,jl}(x_i - x_{ik}) + \Delta y_{ik,jl}(y_i - y_{ik})) - (\Delta z_{ik,jl}\eta) \\
\eta &= \sqrt{(x_i - x_{ik})^2 + (y_i - y_{ik})^2}
\end{aligned}$$

The cost function and its gradient vector, as given by Eqs. (6) and (7), can be used with any inclusion geometry by considering the appropriate set of optimization variables. For example, in the case of circular shapes (z, θ, ϕ) are constant hence gradients vanish corresponding to these variables.

3. Generating RVE of different inclusion shapes

This section demonstrates RVE generation for circular, spherical, four non-circular and four non-spherical inclusion shapes. Fig. 3 shows the UnS form of non-circular and non-spherical inclusion shapes. Generating an RVE requires solving the optimization problem given in Eq. (3). Constraints of Eq. (3) become simple bounds on the spatial variables for box shaped RVE (i.e., rectangle in 2D and cuboid in 3D). Gradient projection methods, an extension of the steepest descent method to the constrained optimization, are proved to be effective choices [36] for solving optimization problems with such simple bounds. Hence, Non-monotone spectral projected gradient (NMSPG) algorithm [37,38], a variant of gradient projection methods, is used to solve the Eq. (3). The particular choice of the algorithm is based on two reasons. One, the speed of convergence due to the choice of spectral step length. Two, guaranteed global convergence due to the non-monotone nature of the line-search. In NMSPG implementation, parameters $M = 50, \alpha_{min} = 10^{-6}, \alpha_{max} = 10^{6}, \sigma_1 = 0.1, \sigma_2 = 0.9, \gamma = 10^{-4}$ are used with the same naming convention as in [37]. RVE generation procedure is designed to restart if the solution does not converge in a predefined number of iterations.

Table 1
RVE parameter sets used in the present study.

	v_f	δ	$R\mu_e$	$R\sigma_e$	d_{ss}
Set 1	0.65	25	6×10^{-6} m	0.0	$0.07\times R\mu_e$
Set 2	0.65	50	6×10^{-6} m	0.0	$0.07\times R\mu_e$
Set 3	0.40	15	6×10^{-6} m	0.0	$0.07\times R\mu_e$

Table 1, lists three different sets of RVE parameters used in the present work. In this table, v_f is the inclusion volume fraction, $(R\mu_e, R\sigma_e)$ are mean and standard deviation of reference circle/sphere radii, $\delta = L/R\mu_e$ is the RVE size, L is RVE side length and d_{ss} is inclusions minimum surface-to-surface distance. Dimensions of different inclusion shapes, see Fig. C.11, are chosen to give the same area/volume as that of the reference circle/sphere so that their RVE generation times can be compared. Although RVEs can be generated for variable inclusion sizes, we have used $R\sigma_e = 0$ to study RVE generation for monodisperse inclusions. This is because the monodisperse case requires more computational effort and have lower jamming limits than those with polydisperse inclusions [13]. Two and three-dimensional RVEs generated using the set 1 and set 3, respectively, are shown in Fig. 4

3.1. RVE generation time.

The RVE generation module is written in the open-source computational language Julia [39] and used on a computer with 1.19 GHz,

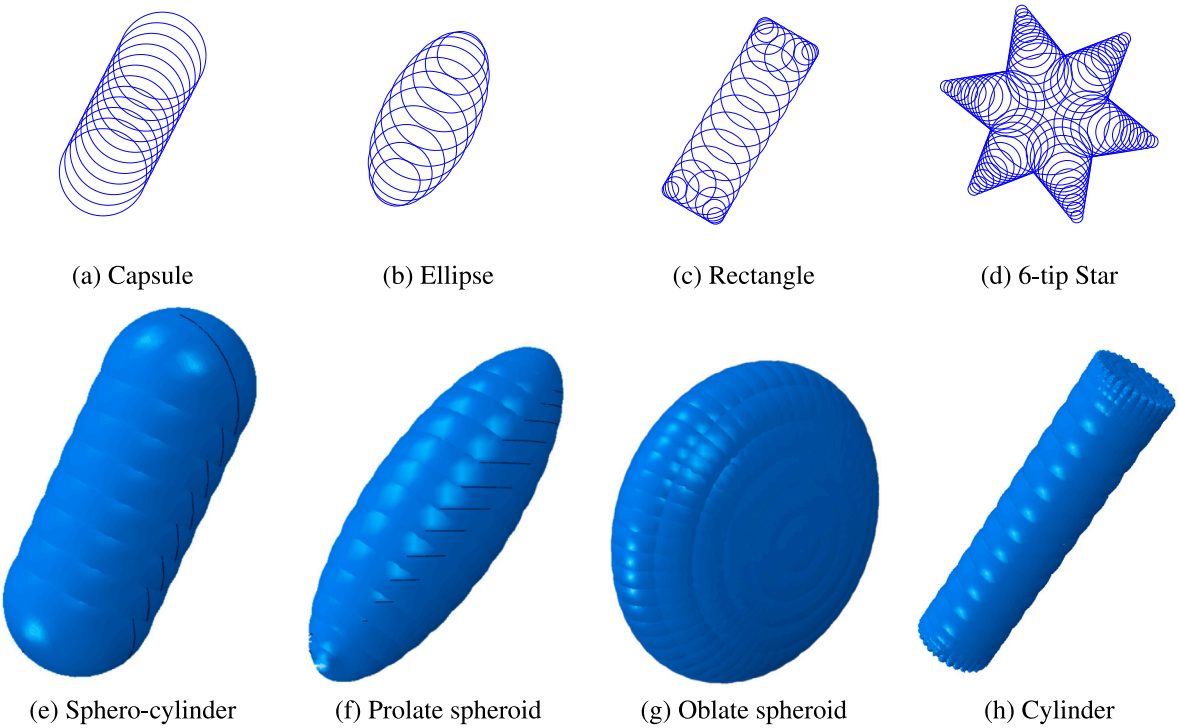

Fig. 3. Non-circular and non-spherical shapes representation as a union of n-Spheres.

four-core, 8 GB RAM specifications. Lower RVE generation times are desirable for producing large data sets which may be used for studying composites with data-hungry approaches like deep learning. To assess the computational performance, RVE generation time study (t_{gen}) is performed with various inclusion shapes having different aspect ratios and RVE sizes (δ). For this purpose, RVE parameters of sets 2 and 3 of Table 1, are used respectively, with $\delta \in \{25, 50, 75, 100\}$ in $2D$ and $\delta \in \{15, 20, 30, 35\}$ in $3D$. It is observed that, a large part of the t_{gen} is due to overlap cost function (f) and its gradient (∇f) evaluations, and it gets enhanced with number of n-Spheres used in UnS form of inclusion(see Section 2.2.1). The f and ∇f are evaluated between a pair of inclusions only if their bounding boxes overlap to avoid unnecessary overlap check with far-off inclusions. This reduces computation costs significantly while dealing with non-convex shapes.

The minimum (t_{min}), mean (t_{μ}), standard deviation (t_{σ}) and maximum (t_{max}) values of t_{gen} are reported for 2D and 3D RVEs of different inclusion shapes in Tables C.5 and C.6, respectively, obtained from 20 realizations in each case of $3D$ RVEs and 50 realizations in each case of $2D$ RVEs. Of all four indicators, meantime is more reliable, as the other metrics are sensitive to outliers. If the random initialization is far from the solution, convergence may not be achieved in the predefined number of iterations, so the RVE generation restarts with new initialization. This leads to higher t_{max} and t_{μ} in some cases. Thus, the parameters $t_{min}, t_{\sigma}, t_{\max}$ can be used to understand the uncertainty involved in that particular case. It is found that t_{gen} is directly proportional to the RVE size and aspect ratio of the inclusion because the increase in RVE size leads to more number of inclusions, and an increase in aspect ratio leads to more chances of inclusion overlap. For n-tip stars, t_{μ} is decreasing from a 3-tip star to a 5-tip star, as the 5-tip star has fewer chances of entanglement/overlap with other inclusions. This is because more tips would result in a smaller tip height for a given star area.

For circle-shaped inclusions, the present algorithm generated RVE of size $\delta = 50$ with 65% inclusion volume fraction in about 0.2–0.3 s, while [13] has reported 107.02 min on a computer with similar specifications. This drastic reduction t_{gen} may be majorly due to explicit gradient evaluation, which otherwise has to be calculated using computationally expensive numerical methods. Recently, [25] has reported RVE generation times for non-circular inclusion shapes. In comparison with this study, for generating the RVE of approximately 2070 elliptical and rectangular inclusions, the present algorithm takes 35 and 20 s, respectively, while [25] has reported 69 and 86 s. Higher t_{gen} of 3D RVEs, compared to 2D RVEs, is due to an increased number of inclusions for a given RVE size and volume fraction. Note that, we have not reported t_{gen} for RVEs of cylinders with $\delta \in \{30, 35\}$ as the total number of spheres in the system (representing all cylinders in RVE) has reached 200,000 to 300,000, thus leading to very high t_{gen}. RVE generation of such shapes can be made faster by developing cost-effective UnS representation in future work.

4. Statistical validation

It is important to assess the distribution of inclusions in the RVE, as it influences the mechanical response and damage initiation. In the following sections, the spatial distribution of inclusions is evaluated in the neighbourhood and at several radial distances about each inclusion. For this purpose, 20 different realizations of RVEs are generated for each inclusion shape, using the parameters given in set 2 (for 2D) and set 3 (for 3D) of Table 1.

4.1. Voronoi regions areas and volumes

The RVE domain is discretized using Voronoi tessellation [40], with inclusions centres as seed points, to demarcate a unique region (hence neighbours) for each inclusion. Voronoi tessellation of a RVE with circular inclusions of 65% volume fraction is shown in Fig. 5(a). The regular arrangement of inclusions generates Voronoi regions with the uniform area (or volume) and equidistant neighbours. So, these metrics are used to determine the randomness in the immediate neighbourhood of the inclusion. Coefficient of variation, mean normalized standard deviation($c_v = \sigma/\mu$), of Voronoi region areas (c_{va}, for $2D$ RVE) and Voronoi region volumes (c_{vv}, for $3D$ RVE) is shown with box plots in Fig. 5. For regular arrangement, $c_{va} = 0$ due to vanishing standard deviation of Voronoi region areas or volumes and higher c_{va} imply more randomness. Table 2 shows good agreement of c_{va} for RVE of circular

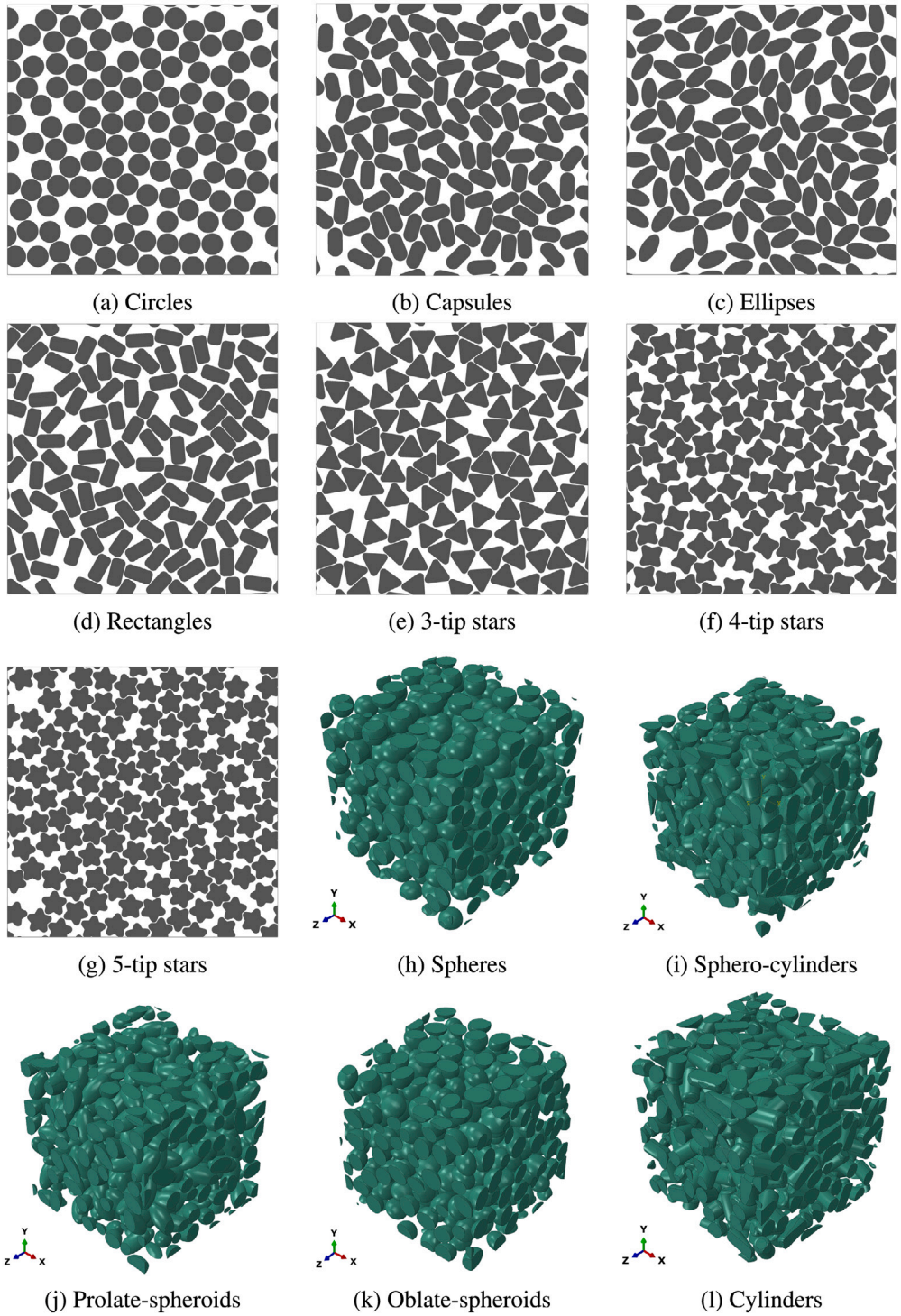

Fig. 4. (a)–(g) 2D RVEs and (h)–(l) 3D RVEs with 65% and 40% inclusion volume fractions respectively.

inclusions when compared with that reported in literature. For the same set of RVE parameters, c_{va} and c_{vv} of all inclusions, except stars, are in the range of 0.1 to 0.15, see Fig. 5, in line with the observations of [22,25]. It is observed that c_{va} is increasing with aspect ratio and decreasing with the number of tips in the case of the n-tip star. As explained previously, a 3-tip star has more chances of entanglement than a 5-tip star.

Table 2
Coefficient of variation of area, c_{va} for RVE of circular inclusions.

	Present algorithm	Pathan et al. [13]	Melro et al. [12]	Wongsto's et al. [21]
$v_f = 56\%$	0.168	0.139	0.137	0.129
$v_f = 65\%$	0.119	0.114	0.099	0.077

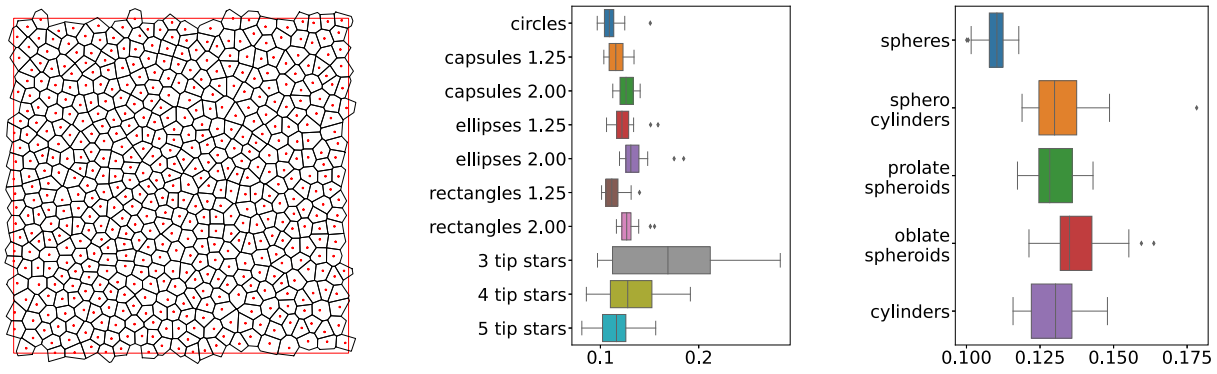

(a) Voronoi tessellation (b) coefficient of variation of area c_{va} (c) coefficient of variation of volume c_{vv}

Fig. 5. A typical Voronoi tessellation and its area and volume metrics for different inclusions.

4.2. Nearest neighbour distributions

In this section, distributions of the first two nearest neighbour distances and nearest neighbour orientation are studied. Probability density functions(PDF) of distances from every inclusion to its closest and second-closest inclusion are plotted, for all the considered inclusion shapes, in Fig. 6. PDFs are determined using kernel density estimation with Gaussian kernel and Scott method based bandwidth. PDF becomes a sharp peak at the neighbour distance if all neighbours are equidistant, as in the case of a regular arrangement. PDF gets flat as the neighbour distance distribution changes from regular to random. Fig. 6 shows such PDF curves flattening with increasing aspect ratio and decreasing number of tips on the star. This further supports previous observations with c_{va}.

Cumulative distribution function (CDF) of nearest neighbour orientations is evaluated, for different inclusion shapes, using kernel density estimation and plotted in Fig. 7. When inclusions are in complete state of randomness (CSR), nearest neighbour angles are expected to take all possible values with equal probability. These angles are evaluated, using Eqs. (1d) and (1e), and plotted on the same Fig. 7. It is observed that, in all three plots of Fig. 7, CDF of different inclusion shapes is closely following that of the CSR. This indicates retained randomness in the nearest neighbour orientations, after the inclusions re-positioning during overlap removal process.

4.3. Ripley's K function, K(r)

Ripley's K function, $K(r)$, determines the expected number of points inside a search circle (or sphere) of radius r, centred at any point i, using the Eq. (8)

$$\mathbb{E}(r) = \lambda K(r) = \frac{1}{n}\sum_{i=1}^{n}\sum_{j\neq i}^{n} I(d_{ij} \leq r) w_{ij}(r) \tag{8}$$

where, λ is point density, n is the number of points and I is the indicator function with value of 1 if the point j is inside the search circle (or sphere), otherwise zero. Edge correction term, $w_{ij}(r)$, factors the absence of points in the exterior part of the search circle (or sphere) if it crosses the bounds of the domain. The edge correction term can be avoided by replicating RVEs around the RVE due to the virtue of its periodicity.

Residual Ripley's K function, $L(r)$, given in Eq. (9) measures the deviation of a given distribution from that of the CSR. In the case of CSR, $K_p(r)$ have πr^2 and $\frac{4}{3}\pi r^3$ for $2D$ and $3D$ RVEs respectively.

$$L(r) = \begin{cases} \sqrt{\dfrac{K(r)}{\pi}} - r, & \text{for 2D case} \\ \sqrt[3]{\dfrac{3K(r)}{4\pi}} - r, & \text{for 3D case} \end{cases} \tag{9}$$

In a search circle (or sphere) of a given radius r, the number of expected points higher than $K_p(r)$ indicates clustering, while the lower number implies dispersion. Hence, $L(r)$ takes the value of zero for CSR distribution and oscillates about zero for a regular arrangement. In Figs. 8(a) and (b), $L(r)$ is plotted for $2D$ and $3D$ cases, with standard deviation error bars, evaluated from 20 realizations. In the case of $2D$ inclusion shapes, $L(r)$ is stabilized at about a radial distance ratio of 7 and remained constant but slightly above zero, indicating minor clustering for longer distances. In the case of $3D$ inclusion shapes, L(r) is not fluctuating but monotonically reduced to zero, indicating the absence of regular arrangement.

4.4. Radial distribution function, G(r)

Ripley's K function evaluates point patterns up to radius r in a cumulative manner. Hence, it becomes difficult to identify the radial distance where the given distribution is deviating from the CSR. For this purpose, the radial distribution function, $G(r)$, given in Eq. (10), is derived from $K(r)$. It evaluates the probability of finding points in a circular strip (or spherical shell) of inner radius r and small thickness dr, centred at any arbitrary point.

$$G(r) = \begin{cases} \dfrac{1}{2\pi r}\dfrac{dK(r)}{dr} = \dfrac{A}{2\pi r dr N^2}\sum_{i=1}^{n} N_i(r, r+dr) & \text{for 2D case} \\ \dfrac{1}{4\pi r^2}\dfrac{dK(r)}{dr} = \dfrac{A}{4\pi r^2 dr N^2}\sum_{i=1}^{n} N_i(r, r+dr) & \text{for 3D case} \end{cases} \tag{10}$$

where, N_i is the number of points in an annulus of inner radius r and outer radius $r + dr$ centred at ith inclusion centre. In the case of CSR, $G(r)$ approaches unity at sufficiently longer distances from the inclusion centre. Radial distribution functions for $2D$ and $3D$ inclusion shapes, evaluated from 20 realizations, is shown in Figs. 8(c) and (d) with standard deviation as error bars. In the case of both $2D$ and $3D$ inclusion shapes, $G(r)$ approaches unity at radial distance ratios of about 7, indicating the randomness at sufficiently longer radial distances.

5. Micro-mechanical validation

In this section, 2D RVEs generated using the proposed algorithm are assessed for transverse isotropy, using finite element based micromechanical analysis. Isotropy is expected on the cross-section normal to fibre direction due to the random distribution of fibres. In order to compare with the literature results, the same RVE parameters and material set E-glass/MY750/HY917/DY063 are considered [41]. Four different inclusion shapes, circle, ellipse, capsule and rectangle, are considered in this analysis. The material set contains linear elastic isotropic matrix and fibre with Young's modulus and Poisson's ratio $E_m = 3.35$ GPa, $\nu_m = 0.35$, $E_f = 74$ GPa, $\nu_f = 0.2$ respectively. RVEs are generated with

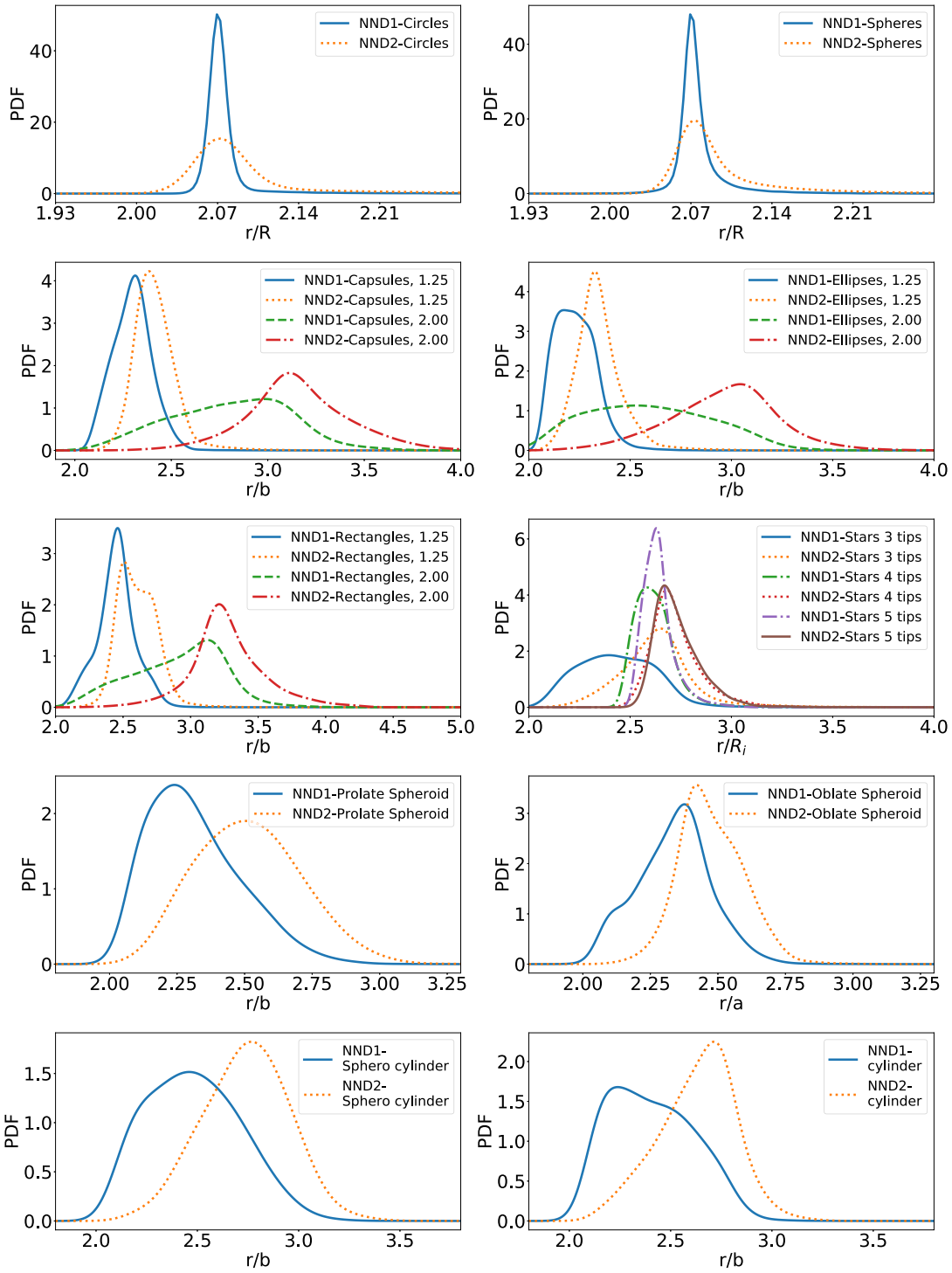

Fig. 6. Probability density function (PDF) of first two nearest neighbour distances of various inclusion shapes.

constant fibre radius $r_f = 2.6$ μm, RVE window size $\delta = 50.0$, $d_{ss} = 0.07r_f$ and inclusion volume fraction $vf \in \{0.2, 0.3, 0.4, 0.5, 0.6\}$. For each vf and inclusion shape, 20 different realizations are generated.

Finite element models of RVE are generated in ABAQUS using python scripts. As we are interested only in transverse properties of the composite, four-node plane strain elements (CPE4), along with a small proportion of three-node triangular elements (CPE3), are used in finite element modelling. The number of elements in each model is chosen as approximately 50,000 elements following a mesh convergence study. Periodic boundary conditions (PBC) are chosen over uniform boundary conditions. This is because, when PBC are applied, equivalent properties of composite converge faster with RVE size [42–44]. PBC are applied on the four edges using dummy nodes (known as reference points in ABAQUS terminology) using the procedure explained in [45].

The effective material properties evaluated from the micromechanical analysis of RVEs, containing 60% volume fraction of circular inclusions, match closely with the values reported in the literature (see Table 3). Also, as shown in Table 4, transverse isotropy is observed in the RVEs of different fibre shapes. In Fig. 9, effective transverse elastic

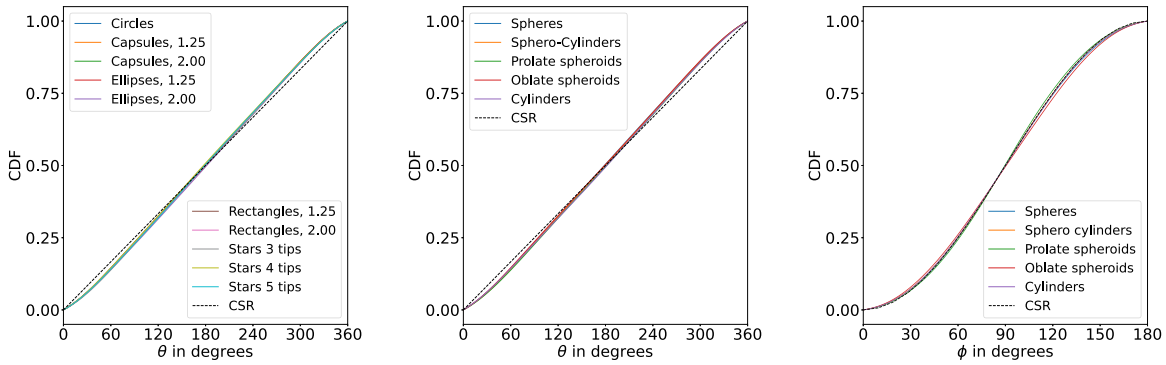

Fig. 7. Cumulative distribution function (CDF) of nearest neighbour orientations, of $2D$ and $3D$ inclusion shapes.

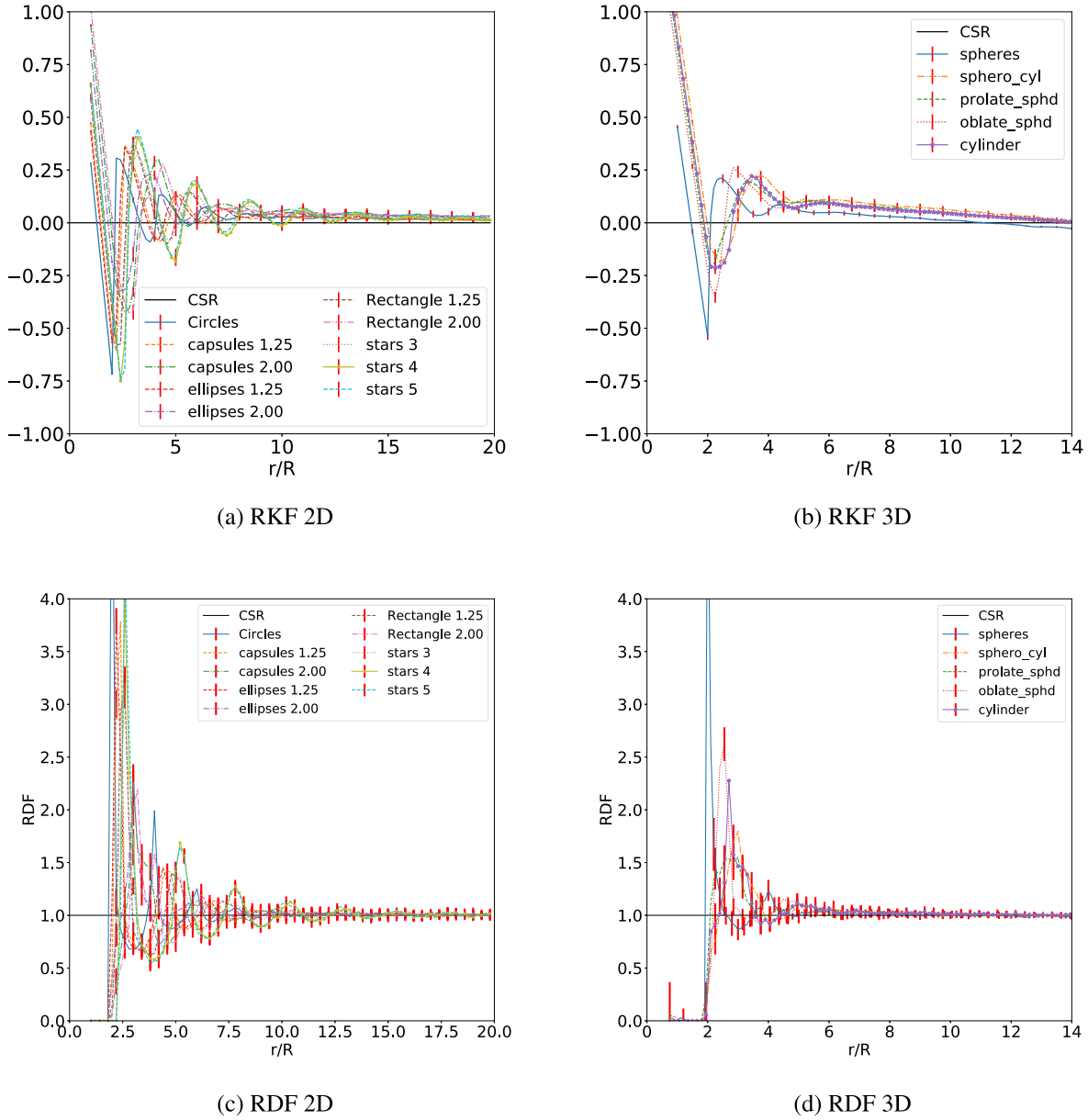

Fig. 8. Long-range metrics, (a–b) residual Ripley's K function, L(r) and (c–d) radial distribution function G(r) for $2D$ and $3D$ inclusion shapes.

Table 3
Transverse effective properties for RVE of circles.

	E_{22}(in GPa)	E_{33} (in GPa)	G_{23} (in GPa)	ν_{23}	ν_{32}
Mean (Std. dev)	13.656(0.126)	13.710(0.24)	4.842(0.08)	0.400(0.007)	0.402(0.004)
Experimental [41]	16.2	16.2	5.786	0.4	0.4
Pathan et al. [13]	13.02	12.927	4.736	0.4037	0.4008
Melro et al. [12]	13.367	13.387	4.851	0.370	0.371

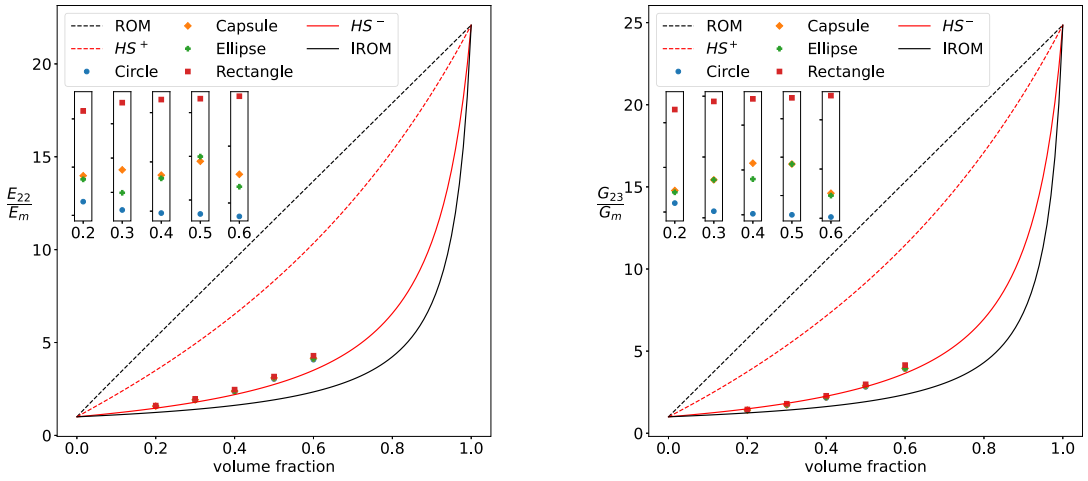

Fig. 9. Transverse elastic and shear moduli for different inclusion shapes.

Table 4
Transverse isotropy for different inclusion shapes, with 60% volume fraction.

Inclusion shape	E_{22}/E_{33}	ν_{23}/ν_{32}	$G_{23}/\frac{E_{22}}{2(1+\nu_{23})}$
Circle	0.9961	0.9955	0.9931
Ellipse	0.9966	0.9983	0.9875
Capsule	0.9956	0.996	0.9933
Rectangle	0.9968	0.9967	0.9981

and shear moduli are plotted for different inclusion shapes of five different volume fractions. It is observed that all the evaluated properties are within the absolute (Voigt–Reuss) bounds and are very close to Hashin–Shtrikman lower bound as expected for transverse properties. Hence, RVEs generated using the proposed algorithm are suitable for modelling the microstructure of the unidirectional composite materials.

6. Conclusions

A computationally efficient method is developed for generating periodic RVEs of arbitrary inclusion shapes. Inclusion overlaps that occurred during random initialization are removed by solving a constrained optimization problem. Overlap detection between arbitrary inclusion shapes is accomplished by representing each of them as a union of n-Spheres(UnS). The following conclusions are drawn from a detailed RVE generation time study, statistical and micromechanical analysis of RVEs. In these studies, ten different inclusion shapes are used and the influence of varying aspect ratios is also considered.

- Repositioning of the inclusions using the proposed overlap cost function gradient had enabled faster RVE generation; gradient yields a coordinated movement of inclusions, by considering the position of their neighbours, to reduce the overall inclusion overlap in the RVE.
- Increasing aspect ratio of the inclusions has increased computational time, lowered the maximum reachable volume fraction due to the increased chances of overlap.
- Statistical analysis of RVEs has shown randomness, both, in the neighbourhood and at longer distances from the inclusion centre.
- Micromechanical analysis of RVEs has shown transverse isotropy for circular, elliptical and rectangular inclusion shapes, indicating the random distribution of inclusion shapes.

Inclusions overlap detection using UnS representation can make the existing RVE generation algorithms handle arbitrary inclusion shapes. Also, UnS representation could be used for object/shape collision detection in other fields like robotics and computer graphics. Due to computational efficiency and capability to work with different inclusion shapes, large and rich/varied data sets of RVEs can be generated for data-driven studies of composite materials.

CRediT authorship contribution statement

Rajesh Nakka: Conceptualization, Methodology, Software, Validation, Investigation, Formal analysis, Writing – original draft. **Dineshkumar Harursampath:** Supervision, Resources, Writing – review & editing. **Mehtab Pathan:** Writing – review & editing. **Sathiskumar A. Ponnusami:** Supervision, Project administration, Writing – review & editing.

Declaration of competing interest

The authors declare that they have no known competing financial interests or personal relationships that could have appeared to influence the work reported in this paper.

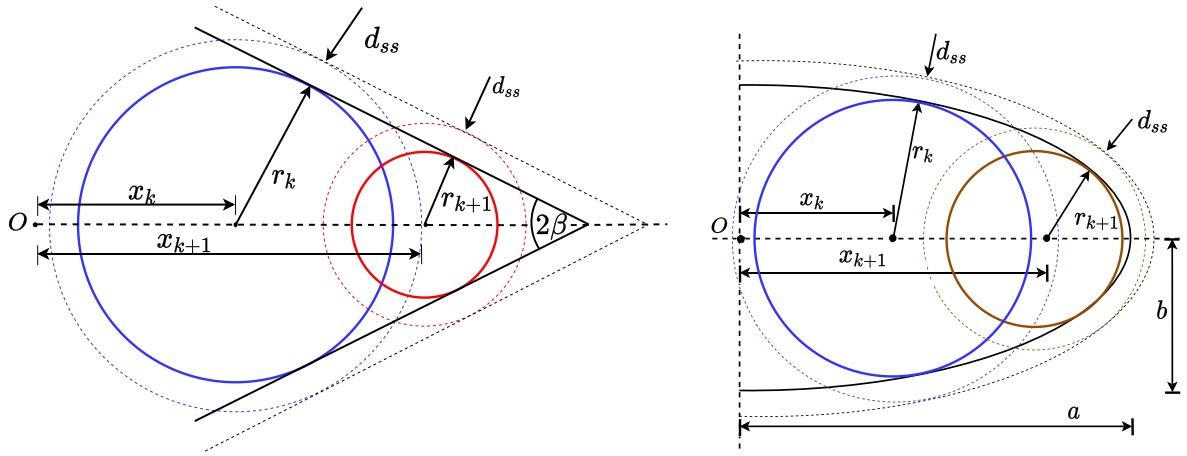

(a) Pair of lines/planes (b) Ellipse/spheroid

Fig. A.10. Schematic representation of n-Spheres arrangement.

Appendix A. Shape representation as a union of n-Spheres

Eqs. (A.1) and (A.2) give successive n-Spheres for representing the region between a pair of lines/planes and ellipse/spheroid, respectively. Fig. A.10 shows the schematic of these n-Spheres arrangement along with the parameters used in Eqs. (A.1) and (A.2). Note that, for the sake of simplicity, n-Spheres position and radii are determined for shapes placed at the origin with its axis aligned with the positive x-axis. Then these n-Spheres are rotated and translated, about the origin, to the actual position of the inclusion. Eq. (A.1), can be used for many standard shapes like n-sided regular polygon (with $\beta = \pi - \frac{2\pi}{n}$ at each corner), capsule (with $\beta = 0$), rectangle (with $\beta = \pi/4$ at each corner and $\beta = 0$ along the axis).

$$\begin{aligned} x_{k+1} &= x_k + \frac{2d_{ss}}{\cos\beta}\left[\sqrt{1+\frac{2r_k}{d_{ss}}} - \tan\beta\right] \\ r_{k+1} &= r_k - (x_{k+1} - x_k)\sin\beta \end{aligned} \tag{A.1}$$

$$\begin{aligned} x_{k+1} &= x_k(2\xi^2 - 1) + 2E\sqrt{(1-\xi^2)r_k^2 + \xi(b+d_{ss})^2 - b^2} \\ r_{k+1} &= \sqrt{b^2 - \left(\frac{x_{k+1}}{e}\right)^2} \end{aligned} \tag{A.2}$$

where, $\xi = E/e$, $E = \sqrt{1 - \frac{(b+d_{ss})^2}{(a+d_{ss})^2}}$, $e = \sqrt{1 - \frac{b^2}{a^2}}$.

Appendix B. Gradient evaluation

The gradient of cost function, f, is evaluated, with respect to an independent variable w_p of the p^{th} inclusion, as follows

$$\frac{\partial f}{\partial w_p} = \frac{\partial}{\partial w_p}\left(\sum_{i=1}^{N-1}\sum_{j=i+1}^{N}\sum_{k=1}^{N_i}\sum_{l=1}^{N_j} C_{ik,jl}^2\right) = 2\sum_{i=1}^{N-1}\sum_{j=i+1}^{N}\sum_{k=1}^{N_i}\sum_{l=1}^{N_j} C_{ik,jl}\frac{\partial C_{ik,jl}}{\partial w_p} \tag{B.1}$$

For the overlap cost, $C_{ik,jl}$ between k^{th} and l^{th} n-Sphere of i^{th} and j^{th} inclusion,

- $C_{ik,jl} = C_{jl,ik}$, as the cost overlap between i and j should be the same as that between j and i.
- $C_{ik,jl} = 0$ for $i = j = p$, as the cost of overlap is defined for a pair of two different inclusions
- $\frac{\partial C_{ik,jl}}{\partial w_p} = 0$ for $i \neq p$ and $j \neq p$, as the overlap magnitude between a pair of inclusions is independent of other inclusions position

using the above properties of $C_{ik,jl}$, Eq. (B.1), is simplified as,

$$\frac{\partial f}{\partial w_p} = 2\sum_{i=1}^{p-1}\sum_{k=1}^{N_i}\sum_{l=1}^{N_j} C_{ik,pl}\frac{\partial C_{ik,pl}}{\partial w_p} + 2\sum_{j=p+1}^{N}\sum_{k=1}^{N_i}\sum_{l=1}^{N_j} C_{pk,jl}\frac{\partial C_{pk,jl}}{\partial w_p} \tag{B.2}$$

In the first term, replacing i with j and using $C_{ik,jl} = C_{jl,ik}$ gives,

$$\frac{\partial f}{\partial w_p} = 2\sum_{\substack{j=1\\ \neq p}}^{N}\sum_{k=1}^{N_i}\sum_{l=1}^{N_j} C_{pk,jl}\frac{\partial C_{pk,jl}}{\partial w_p} \tag{B.3}$$

Now, using i to represent any inclusion instead of p,

$$\boxed{\frac{\partial f}{\partial w_i} = 2\sum_{\substack{j=1\\ \neq i}}^{N}\sum_{k=1}^{N_i}\sum_{l=1}^{N_j} C_{ik,jl}\frac{\partial C_{ik,jl}}{\partial w_i}} \tag{B.4}$$

using Eq. (4) in Eq. (B.4),

$$\begin{aligned} \frac{\partial f}{\partial w_i} &= 2\sum_{\substack{j=1\\ \neq i}}^{N}\sum_{k=1}^{N_i}\sum_{l=1}^{N_j}(\overline{d_{ik,jl}} - d_{ik,jl})\left(\frac{\partial \overline{d_{ik,jl}}}{\partial w_i} - \frac{\partial d_{ik,jl}}{\partial w_i}\right)\mathbf{H}[\overline{d_{ik,jl}} - d_{ik,jl}] \\ &= -2\sum_{\substack{j=1\\ \neq i}}^{N}\sum_{k=1}^{N_i}\sum_{l=1}^{N_j} C_{ik,jl}\frac{\partial d_{ik,jl}}{\partial w_i} \end{aligned} \tag{B.5}$$

Using Eq. (5) in Eq. (B.5) gives the cost function gradient as shown in Eq. (7).

Appendix C. Geometry of shapes

See Fig. C.11 for geometry details of inclusion shapes.

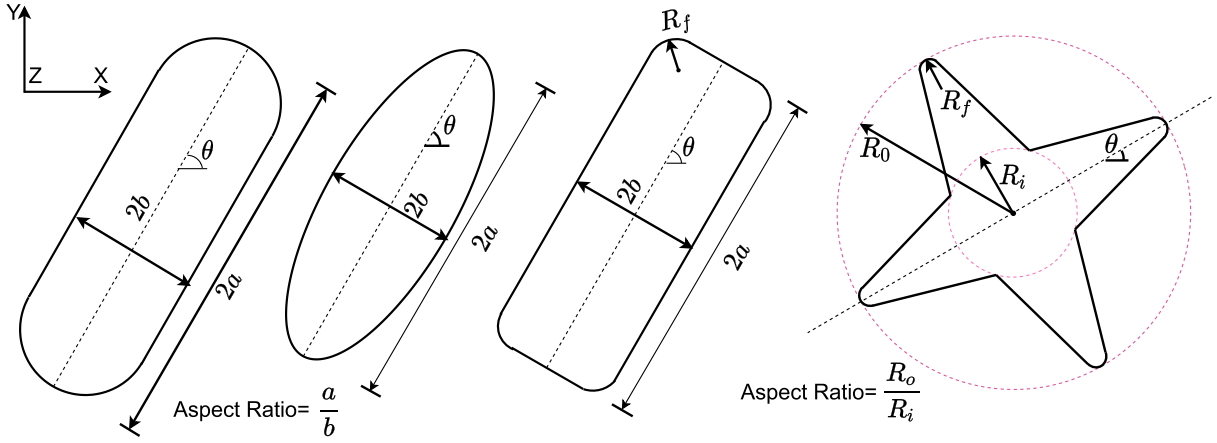

Fig. C.11. Geometrical details of inclusion shapes.

Table C.5
RVE generation times (in seconds) for different 2D inclusion shapes, with different RVE size δ and number of inclusions N_{inc}.

		Circle	Capsule		Ellipse		Rectangle		Star		
			$AR = a/b$		$AR = a/b$		$AR = a/b$		n = 3	n = 4	n = 5
			1.25	2.0	1.25	2.0	1.25	2.0			
	t_{min}	0.01	0.02	0.04	0.05	0.06	0.09	0.29	0.17	0.24	0.21
$\delta = 25$	t_{μ}	0.02	0.04	0.16	0.10	0.18	0.24	1.58	0.64	0.53	0.48
$N_{inc} \approx 130$	t_{σ}	0.05	0.03	0.33	0.05	0.08	0.11	1.86	0.33	0.33	0.2
	t_{max}	0.37	0.20	2.42	0.34	0.39	0.79	10.09	1.74	2.25	1.18
	t_{min}	0.12	0.19	0.44	0.39	0.71	0.57	2.68	2.07	2.11	1.89
$\delta = 50$	t_{μ}	0.22	0.37	1.49	0.88	2.47	1.93	9.41	26.22	7.00	4.72
$N_{inc} \approx 520$	t_{σ}	0.1	0.17	2.53	0.43	3.54	1.0	6.74	48.39	4.31	2.72
	t_{max}	0.56	1.12	18.55	2.57	26.41	5.84	32.92	250.0	23.22	12.0
	t_{min}	0.49	0.84	2.13	1.70	2.81	2.32	9.66	7.03	5.60	5.34
$\delta = 75$	t_{μ}	0.84	2.31	7.97	5.37	10.31	8.44	43.54	106.43	47.22	24.01
$N_{inc} \approx 1170$	t_{σ}	0.51	1.49	11.46	2.52	5.89	17.21	32.92	159.39	76.47	21.07
	t_{max}	3.11	6.49	82.1	10.72	31.0	126.11	155.48	763.54	509.15	65.18
	t_{min}	1.30	2.30	5.0	4.70	5.67	7.60	49.65	21.42	19.49	19.75
$\delta = 100$	t_{μ}	2.43	5.87	36.1	15.44	35.55	20.99	253.74	278.86	232.34	140.87
$N_{inc} \approx 2070$	t_{σ}	1.37	4.88	50.57	13.75	28.37	17.57	188.32	271.36	313.97	191.71
	t_{max}	11.11	29.59	347.16	70.11	111.12	94.93	856.15	1451.25	1258.27	1333.78

Table C.6
RVE generation times (in seconds) for 3D inclusion shapes, with different RVE size δ and number of inclusions N_{inc}.

		Sphere	Sphero-cylinder	Spheroid		Cylinder
			AR = a/b	$AR = a/b$		$AR = a/b$
			2.0	0.75	2.0	2.0
	t_{min}	0.1	0.56	0.79	1.79	160.0
$\delta = 15$	t_{μ}	0.18	8.75	2.36	2.42	470.23
$N_{inc} \approx 323$	t_{σ}	0.08	2.54	1.34	0.52	269.5
	t_{max}	0.47	26.48	5.96	3.29	1471.4
	t_{min}	0.40	4.2	3.39	7.68	526.74
$\delta = 20$	t_{μ}	0.62	40.7	8.34	16.82	1166.9
$N_{inc} \approx 764$	t_{σ}	0.17	20.01	4.66	8.11	190.0
	t_{max}	1.13	94.77	21.03	40.93	1589.1
	t_{min}	3.91	184.23	32.88	73.84	–
$\delta = 30$	t_{μ}	5.11	405.21	92.69	206.4	–
$N_{inc} \approx 2579$	t_{σ}	0.82	90.77	30.25	110.4	–
	t_{max}	6.51	590.61	201.57	412.05	–
	t_{min}	9.24	227.2	60.11	169.4	–
$\delta = 35$	t_{μ}	12.99	709.7	361.28	526.46	–
$N_{inc} \approx 4095$	t_{σ}	2.51	180.9	200.26	120.54	–
	t_{max}	17.19	1102.4	756.06	1127.5	–

References

[1] Brockenbrough J, Suresh S, Wienecke H. Deformation of metal-matrix composites with continuous fibers: geometrical effects of fiber distribution and shape. Acta Metall Mater 1991;39(5):735–52. http://dx.doi.org/10.1016/0956-7151(91)90274-5, URL https://www.sciencedirect.com/science/article/pii/0956715191902745.

[2] Pyrz R. Correlation of microstructure variability and local stress field in two-phase materials. Mater Sci Eng A 1994;177(1):253–9. http://dx.doi.org/10.1016/0921-5093(94)90497-9, URL http://www.sciencedirect.com/science/article/pii/0921509394904979.

[3] Pyrz R. Quantitative description of the microstructure of composites. Part I: Morphology of unidirectional composite systems. Compos Sci Technol 1994;50(2):197–208. http://dx.doi.org/10.1016/0266-3538(94)90141-4, URL http://www.sciencedirect.com/science/article/pii/0266353894901414.

[4] Beicha D, Kanit T, Brunet Y, Imad A, Moumen AE, Khelfaoui Y. Effective transverse elastic properties of unidirectional fiber reinforced composites. Mech Mater 2016;102:47–53. http://dx.doi.org/10.1016/j.mechmat.2016.08.010, URL https://www.sciencedirect.com/science/article/pii/S0167663616302241.

[5] Ahmadian H, Yang M, Nagarajan A, Soghrati S. Effects of shape and misalignment of fibers on the failure response of carbon fiber reinforced polymers. Comput Mech 2018;63(5):999–1017. http://dx.doi.org/10.1007/s00466-018-1634-1.

[6] TRIAS D, COSTA J, TURON A, HURTADO J. Determination of the critical size of a statistical representative volume element (SRVE) for carbon reinforced polymers. Acta Mater 2006;54(13):3471–84. http://dx.doi.org/10.1016/j.actamat.2006.03.042.

[7] Hoang TH, Guerich M, Yvonnet J. Determining the size of RVE for nonlinear random composites in an incremental computational homogenization framework. J Eng Mech 2016;142(5):04016018. http://dx.doi.org/10.1061/(asce)em.1943-7889.0001057.

[8] Bargmann S, Klusemann B, Markmann J, Schnabel JE, Schneider K, Soyarslan C, Wilmers J. Generation of 3D representative volume elements for heterogeneous materials: A review. Prog Mater Sci 2018;96:322–84. http://dx.doi.org/10.1016/j.pmatsci.2018.02.003, URL http://www.sciencedirect.com/science/article/pii/S0079642518300161.

[9] Louis P, Gokhale AM. Application of image analysis for characterization of spatial arrangements of features in microstructure. Metall Mater Trans A 1995;26(6):1449–56. http://dx.doi.org/10.1007/BF02647595, URL https://doi.org/10.1007/BF02647595.

[10] Yamamoto S, Matsuoka T. Dynamic simulation of microstructure and rheology of fiber suspensions. Polym Eng Sci 1996;36(19):2396–403. http://dx.doi.org/10.1002/pen.10638, arXiv:https://onlinelibrary.wiley.com/doi/pdf/10.1002/pen.10638, URL https://onlinelibrary.wiley.com/doi/abs/10.1002/pen.10638.

[11] Park JM, Park SJ. Modeling and simulation of fiber orientation in injection molding of polymer composites. Math Probl Eng 2011;2011:1–14. http://dx.doi.org/10.1155/2011/105637.

[12] Melro A, Camanho P, Pinho S. Generation of random distribution of fibres in long-fibre reinforced composites. Compos Sci Technol 2008;68(9):2092–102. http://dx.doi.org/10.1016/j.compscitech.2008.03.013, URL http://www.sciencedirect.com/science/article/pii/S0266353808001048.

[13] Pathan M, Tagarielli V, Patsias S, Baiz-Villafranca P. A new algorithm to generate representative volume elements of composites with cylindrical or spherical fillers. Composites B 2017;110:267–78. http://dx.doi.org/10.1016/j.compositesb.2016.10.078, URL http://www.sciencedirect.com/science/article/pii/S1359836816313725.

[14] Feder J. Random sequential adsorption. J Theoret Biol 1980;87(2):237–54. http://dx.doi.org/10.1016/0022-5193(80)90358-6, URL https://www.sciencedirect.com/science/article/pii/0022519380903586.

[15] Torquato S, Uche OU, Stillinger FH. Random sequential addition of hard spheres in high euclidean dimensions. Phys Rev E 2006;74(6). http://dx.doi.org/10.1103/physreve.74.061308.

[16] Cooper DW. Random-sequential-packing simulations in three dimensions for spheres. Phys Rev A 1988;38:522–4. http://dx.doi.org/10.1103/PhysRevA.38.522, URL https://link.aps.org/doi/10.1103/PhysRevA.38.522.

[17] Buryachenko V, Pagano N, Kim R, Spowart J. Quantitative description and numerical simulation of random microstructures of composites and their effective elastic moduli. Int J Solids Struct 2003;40(1):47–72. http://dx.doi.org/10.1016/S0020-7683(02)00462-6, URL http://www.sciencedirect.com/science/article/pii/S0020768302004626.

[18] Tian W, Chao X, Fu M, Qi L. An algorithm for generation of RVEs of composites with high particle volume fractions. Compos Sci Technol 2021;207:108714. http://dx.doi.org/10.1016/j.compscitech.2021.108714, URL https://www.sciencedirect.com/science/article/pii/S0266353821000701.

[19] Vaughan T, McCarthy C. A combined experimental–numerical approach for generating statistically equivalent fibre distributions for high strength laminated composite materials. Compos Sci Technol 2010;70(2):291–7. http://dx.doi.org/10.1016/j.compscitech.2009.10.020, URL http://www.sciencedirect.com/science/article/pii/S0266353809003832.

[20] Yang L, Yan Y, Ran Z, Liu Y. A new method for generating random fibre distributions for fibre reinforced composites. Compos Sci Technol 2013;76:14–20. http://dx.doi.org/10.1016/j.compscitech.2012.12.001, URL http://www.sciencedirect.com/science/article/pii/S0266353812004083.

[21] Wongsto A, Li S. Micromechanical FE analysis of UD fibre-reinforced composites with fibres distributed at random over the transverse cross-section. Composites A 2005;36(9):1246–66. http://dx.doi.org/10.1016/j.compositesa.2005.01.010, URL http://www.sciencedirect.com/science/article/pii/S1359835X05000485.

[22] Catalanotti G. On the generation of RVE-based models of composites reinforced with long fibres or spherical particles. Compos Struct 2016;138:84–95. http://dx.doi.org/10.1016/j.compstruct.2015.11.039, URL https://www.sciencedirect.com/science/article/pii/S0263822315010429.

[23] Zhang T, Yan Y. A comparison between random model and periodic model for fiber-reinforced composites based on a new method for generating fiber distributions. Polym Compos 2017;38(1):77–86. http://dx.doi.org/10.1002/pc.23562, arXiv:https://onlinelibrary.wiley.com/doi/pdf/10.1002/pc.23562, URL https://onlinelibrary.wiley.com/doi/abs/10.1002/pc.23562.

[24] Ge W, Wang L, Sun Y, Liu X. An efficient method to generate random distribution of fibers in continuous fiber reinforced composites. Polym Compos 2019;40(12):4763–70. http://dx.doi.org/10.1002/pc.25344, arXiv:https://onlinelibrary.wiley.com/doi/pdf/10.1002/pc.25344, URL https://onlinelibrary.wiley.com/doi/abs/10.1002/pc.25344.

[25] Herráez M, Segurado J, González C, Lopes C. A microstructures generation tool for virtual ply property screening of hybrid composites with high volume fractions of non-circular fibers – VIPER. Composites A 2020;129:105691. http://dx.doi.org/10.1016/j.compositesa.2019.105691, URL https://www.sciencedirect.com/science/article/pii/S1359835X19304403.

[26] Wang W, Wang J, Kim M-S. An algebraic condition for the separation of two ellipsoids. Comput Aided Geom Design 2001;18(6):531–9. http://dx.doi.org/10.1016/S0167-8396(01)00049-8, URL https://www.sciencedirect.com/science/article/pii/S0167839601000498.

[27] Zheng X, Palffy-Muhoray P. Distance of closest approach of two arbitrary hard ellipses in two dimensions. Phys Rev E 2007;75:061709. http://dx.doi.org/10.1103/PhysRevE.75.061709.

[28] Gilbert E, Johnson D, Keerthi S. A fast procedure for computing the distance between complex objects in three-dimensional space. IEEE J Robot Autom 1988;4(2):193–203. http://dx.doi.org/10.1109/56.2083.

[29] Chen Q, Tu W, Ma M. Deep learning in heterogeneous materials: Targeting the thermo-mechanical response of unidirectional composites. J Appl Phys 2020;127(17):175101. http://dx.doi.org/10.1063/5.0002917, arXiv:https://doi.org/10.1063/5.0002917.

[30] Rao C, Liu Y. Three-dimensional convolutional neural network (3D-CNN) for heterogeneous material homogenization. 2020, CoRR, URL arXiv:2002.07600.

[31] Pathan MV, Ponnusami SA, Pathan J, Pitisongsawat R, Erice B, Petrinic N, Tagarielli VL. Predictions of the mechanical properties of unidirectional fibre composites by supervised machine learning. Sci Rep 2019;9(1):13964. http://dx.doi.org/10.1038/s41598-019-50144-w.

[32] Ye S, Li B, Li Q, Zhao H-P, Feng X-Q. Deep neural network method for predicting the mechanical properties of composites. Appl Phys Lett 2019;115(16):161901. http://dx.doi.org/10.1063/1.5124529, arXiv:https://doi.org/10.1063/1.5124529.

[33] Weisstein EW. Sphere point picking. 2021, Accessed: 2021-04-30, https://mathworld.wolfram.com/SpherePointPicking.html.

[34] Denisiewicz A, Kuczma M, Kula K, Socha T. Influence of boundary conditions on numerical homogenization of high performance concrete. Materials 2021;14(4). http://dx.doi.org/10.3390/ma14041009, URL https://www.mdpi.com/1996-1944/14/4/1009.

[35] Sun CT, Vaidya RS. Prediction of composite properties from a representative volume element. Compos Sci Technol 1996;56(2):171–9. http://dx.doi.org/10.1016/0266-3538(95)00141-7.

[36] Wang C, Xiu N. Convergence of the gradient projection method for generalized convex minimization. Comput Optim Appl 2000;16(2):111–20. http://dx.doi.org/10.1023/A:1008714607737.

[37] Birgin EG, Martínez JM, Raydan M. Nonmonotone spectral projected gradient methods on convex sets. SIAM J Optim 2000;10(4):1196–211. http://dx.doi.org/10.1137/S1052623497330963, arXiv:https://doi.org/10.1137/S1052623497330963.

[38] Birgin E, Martínez J, Raydan M. Spectral projected gradient methods: Review and perspectives. J Stat Softw Articles 2014;60(3):1–21. http://dx.doi.org/10.18637/jss.v060.i03, URL https://www.jstatsoft.org/v060/i03.

[39] Bezanson J, Edelman A, Karpinski S, Shah VB. Julia: A fresh approach to numerical computing. SIAM Rev 2017;59(1):65–98. http://dx.doi.org/10.1137/141000671.

[40] Barber CB, Dobkin DP, Huhdanpaa H. The quickhull algorithm for convex hulls. ACM Trans Math Software 1996;22(4):469–83. http://dx.doi.org/10.1145/235815.235821.

[41] Soden P, Hinton M, Kaddour A. Lamina properties, lay-up configurations and loading conditions for a range of fibre-reinforced composite laminates. Compos Sci Technol 1998;58(7):1011–22. http://dx.doi.org/10.1016/S0266-3538(98)00078-5, URL https://www.sciencedirect.com/science/article/pii/S0266353898000785.

[42] Kanit T, Forest S, Galliet I, Mounoury V, Jeulin D. Determination of the size of the representative volume element for random composites: statistical and numerical approach. Int J Solids Struct 2003;40(13):3647–79. http://dx.doi.org/10.1016/S0020-7683(03)00143-4, URL https://www.sciencedirect.com/science/article/pii/S0020768303001434.

[43] Sab K, Nedjar B. Periodization of random media and representative volume element size for linear composites. Comptes R Mécanique 2005;333(2):187–95. http://dx.doi.org/10.1016/j.crme.2004.10.003, URL https://www.sciencedirect.com/science/article/pii/S1631072104002256.

[44] Moumen AE, Kanit T, Imad A, Minor HE. Effect of overlapping inclusions on effective elastic properties of composites. Mech Res Commun 2013;53:24–30. http://dx.doi.org/10.1016/j.mechrescom.2013.07.007, URL https://www.sciencedirect.com/science/article/pii/S0093641313001092.

[45] Melro A, Camanho P, Andrade Pires F, Pinho S. Micromechanical analysis of polymer composites reinforced by unidirectional fibres: Part II – micromechanical analyses. Int J Solids Struct 2013;50(11):1906–15. http://dx.doi.org/10.1016/j.ijsolstr.2013.02.007, URL https://www.sciencedirect.com/science/article/pii/S0020768313000723.